energies

MDPI

Article

Energy, Exergy, and Economic Performance Comparison and Parametric Optimization of Organic Rankine Cycles Using Isobutane, Isopentane, and Their Mixtures for Waste Heat Recovery

Junsheng Feng [1,*], Yaru Yan [1], Liang Zhao [2] and Hui Dong [2,*]

[1] School of Environment and Energy Engineering, Anhui Jianzhu University, Hefei 230601, China; aurora@stu.ahjzu.edu.cn
[2] School of Metallurgy, Northeastern University, Shenyang 110819, China; zhaoliang1@smm.neu.edu.cn
* Correspondence: fjsheng@ahjzu.edu.cn (J.F.); dongh@mail.neu.edu.cn (H.D.); Tel.: +86-551-6382-8252 (J.F.)

Abstract: The possibility of applying the organic Rankine cycle (ORC) to further recycle the low-grade waste heat efficiently is studied in the present work. The energy, exergy, and economic models of the ORC system are established, and the isobutane, isopentane, and their mixtures are selected as the organic working mediums (OWMs). Due to the slip characteristics of mixed OWM, four operational conditions of the ORC system are proposed, and then the contrastive analysis of energy, exergy, and economic performances under the four operational conditions are conducted. Finally, the optimal mixture mass fraction and crucial parameters of the ORC system are separately determined through the bi-objective optimization. The results show that the ORC system using the mixed OWM can achieve a larger net power output and exergy efficiency by comparing the pure OWM when the condensing temperature is set as the saturated vapor temperature during the condensation process. The electricity production cost first rises and then decreases with the rising mass fraction of isobutane in mixed OWM, and the ORC system using the isopentane can achieve the smallest electricity production cost. By taking the low-grade flue gas of 433.15 K as the ORC heat source, four operational conditions have the same optimal ORC crucial parameters, namely the evaporating temperature of 393.15 K, condensing temperature of 308.15 K, and superheat degree of 0 K. The pure OWM of isobutane can achieve better overall performance by setting the condensing temperature as the saturated liquid temperature.

Keywords: waste heat recovery; organic Rankine cycle; mixed working fluid; exergy efficiency; electricity production cost; parametric optimization

check for updates

Citation: Feng, J.; Yan, Y.; Zhao, L.; Dong, H. Energy, Exergy, and Economic Performance Comparison and Parametric Optimization of Organic Rankine Cycles Using Isobutane, Isopentane, and Their Mixtures for Waste Heat Recovery. *Energies* **2024**, *17*, 5893. https://doi.org/10.3390/en17235893

Academic Editors: Ron Zevenhoven, Panpan Song and Ran Tian

Received: 4 October 2024
Revised: 15 November 2024
Accepted: 22 November 2024
Published: 24 November 2024

1. Introduction

Industrial waste heat recovery (WHR) can effectively improve energy efficiency, reduce greenhouse gas emissions, and play an important role in promoting sustainable development and resource recycling [1]. As the world's largest steel producer and carbon emitter, China is also actively promoting the realization of the "dual carbon" goal [2]. Academician Yin pointed out that the carbon reduction potential of sinter WHR accounted for about 15% of the carbon reduction potential of total WHR in China's steel enterprises [3]. At present, China's iron and steel industry contains abundant sintering low-temperature waste heat resources, but the flue gas waste heat below 200 °C in the sinter waste heat recovery process will be directly discharged into the atmosphere, resulting in a low WHR rate [4]. Strengthening the WHR has been proven to be one of the critical ways for enhancing energy utilization efficiency, which is incorporated into the "14th Five-Year Plan for Industrial Green Development". Therefore, improving the WHR rate of low-grade flue gas (LFG) has a far-reaching impact on realizing the green transformation of the steel industry and promoting resource recycling.

With the continuous improvement of energy efficiency and environmental protection requirements, novel technologies for power generation through WHR from LFG, such as the organic Rankine cycle (ORC) [5], trilateral flash cycle [6], and Karina cycle [7], have broad application prospects in the industrial field. Among them, the ORC has attracted considerable attention due to its simple structure, wide temperature adaptability, and the flexibility in configuring unit capacity [8–12]. In recent years, numerous experts, both domestically and internationally, have carried out extensive research on the ORC system for WHR, and the related research mainly focused on the selection of organic working medium (OWM), energy, exergy, and economic performance analysis, as well as the multi-objective optimization of ORC systems using pure OWM [13–19]. Wang et al. [13] employed exergy analysis to assess exergy destruction across various heat source temperatures and pure OWMs, discovering that those with higher vaporization latent heat, lower critical temperatures, and lower specific liquid heat were particularly well-suited for use in ORC systems. Fergani et al. [16] carried out the exergy, economic, and environmental analyses of the ORC system with three pure OWMs and performed the parameter optimization to achieve the system's optimal operating conditions. Mohammadkhani and Yari [18] and Ping et al. [19] utilized a dual-loop ORC system to examine the temperature distributions and pinch point locations in heat exchangers and analyzed the influences of engine speed and other crucial parameters on the system performance under different pure OWMs. Furthermore, the ORC systems assisted with the Brayton cycle, heat pump, and Kalina cycle for the WHR under different pure OWMs were also investigated [20–22].

The mixed OWMs are created by blending two or more pure OWMs in different mass fractions, allowing for better thermal performance matching and thus improving the thermal efficiency of the system. With the continuous development of ORC power generation technology, researchers both domestically and internationally have begun to explore the use of OWMs in ORC power generation systems [23–31]. Among them, Li et al. [25] studied the combined cooling, heating, and power system using R245fa/R134a as the circulating OWM, and the performance coefficients of the mixed OWM reached 1.35 and 1.39 in the combined cooling and heating mode and the combined cooling, heating, and power mode, respectively, which were significantly higher than those of the pure OWM. Pang et al. [26] and Feng et al. [27] examined the energy, exergy, and economic performances of ORC systems that employed R245fa, R123, and their mixtures while also analyzing how different mass fractions influenced the performance of the system. Dong et al. [29] performed a comprehensive evaluation of the thermodynamic and economic performances of ORC systems using various pure OWMs and their zeotropic mixtures. Miao et al. [31] constructed an optimization index for the physical properties of OWMs coupled with cold and heat source boundary conditions and zeotropic mixtures, so as to avoid the heavy work caused by a large number of system performance calculations. Additionally, researchers have focused on the ORC power generation system using zeotropic mixed OWM, conducting relevant studies on mixture selection, performance analysis, and parameter optimization [32–37].

It can be inferred from the above literature that the flow rate and temperature of the heat source have a significant impact on the energy, exergy, and economic performance of the ORC system [38], resulting in considerable limitations in the applicability of previous research findings to the current ORC system. Moreover, the mixed OWM exhibits temperature glide characteristics during the evaporation and condensation processes. The state location selection of evaporating temperature (ET) and condensing temperature (CT) of OWM had four operational conditions, but the current research of the ORC system utilizing mixed OWM mainly set the saturated liquid temperature during the evaporation and condensation processes as the ET and CT of OWM without considering the saturated vapor temperature, and the effect of state location variation under four operational conditions on the system performance was not analyzed. At present, the ORC system driven by the LFG in the WHR process of sinter only focused on the study of pure OWMs [39–41]. To the authors' knowledge, there have been no studies conducted on ORC systems utilizing mixed OWM for WHR from sintering processes.

In essence, the LFG in the WHR process of sinter is the air of 120–200 °C, and there is no dew point corrosion even if the flue gas temperature is lower, which can be used again for power generation. Therefore, the LFG emitted from the sinter waste heat boiler has been selected as the heat source for the ORC in this study, and four operational conditions of the ORC system using mixed OWM are determined by considering the state location variation of ET and CT of OWM. In addition, then, the energy, exergy, and economic models of the ORC system under four operational conditions are established, and the effects of mixture mass fraction and ORC crucial parameters on the energy, exergy, and economic performances under four operational conditions are analyzed and compared. Finally, the optimal mixture mass fraction and key ORC parameters under the four operational conditions are identified through bi-objective optimization, using exergy and economic performance as the evaluation indexes. The above investigation results have very important guiding significance for using ORC to carry out the WHR of LFG efficiently in the steel industry.

2. System Modeling

2.1. System Description

The ORC power generation system consists of an evaporator, a condenser, an expander, and a working fluid pump, as shown in Figure 1. The OWM absorbs heat in the evaporator to become superheated vapor, which performs work in the expander, then the exhaust vapor is cooled into a liquid in the condenser, and after being pressurized by the working fluid pump, it is sent back to the evaporator, completing the cycle. In the order of 5–1–2–4–5, the ORC system will realize the recovery of low-temperature flue gas and the generation of electricity.

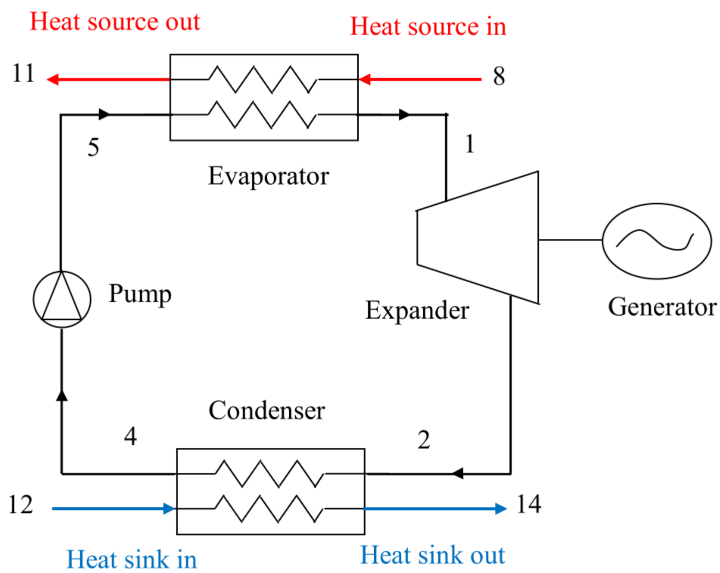

Figure 1. Schematic diagram of ORC system for WHR.

The temperature entropy (T-s) diagrams of the subcritical ORC system with pure OWM and zeotropic mixed OWM are shown in Figure 2a,b, the red and blue lines represent the LFG and cooling water, respectively, and each state point in the figure corresponds to the inlet and outlet positions in Figure 1. As can be seen in Figure 2, the ORC system is composed of four thermal processes: constant pressure heating process (5–1), adiabatic expansion process (1–2), constant pressure cooling process (2–4), and adiabatic pressurization process (4–5). In addition, the process (1–2 s) represents the isentropic expansion of the OWM within the expander, while the process (4–5 s) corresponds to the isentropic compression of the OWM in the pump. Due to the irreversible losses present in both the expander and the pump, the isentropic efficiency of the expander (η_e) and the isentropic efficiency of the pump (η_p) have been predefined. When the superheat degree (SD) of the OWM (ΔT_{sup})

is zero, the OWM at the outlet of the evaporator is in a saturated vapor state. Furthermore, the temperature difference between point 10 and point 6 ($\Delta T_{6\text{-}10}$) represents the minimum heat exchanging temperature difference in the evaporator, while the temperature difference between point 3 and point 13 ($\Delta T_{3\text{-}13}$) indicates the minimum heat exchanging temperature difference in the condenser.

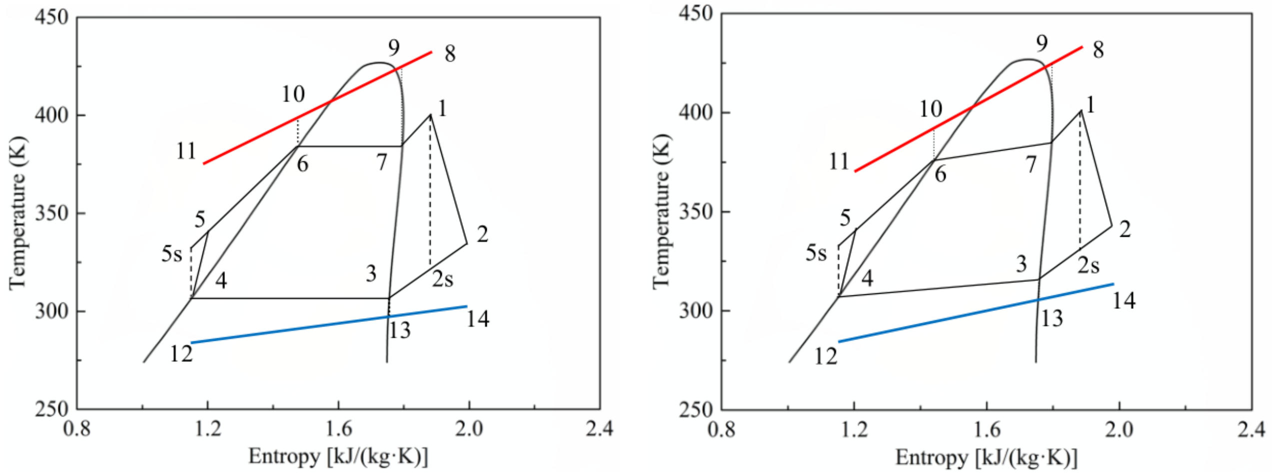

(**a**) Pure OWM (**b**) Mixed OWM

Figure 2. *T-s* diagrams of ORC system using pure and mixed OWMs.

As can be seen in Figure 2a, the evaporation process and condensation process of pure OWM are isothermal, and in order to avoid crossover of temperature distribution in the heat transfer process, it is necessary to apply a limit on the temperature difference between the pinch points, resulting in the temperature difference between the cold and hot ends of the heat exchanger being limited. The zeotropic mixed OWM exhibits a temperature glide phenomenon during the phase change process, which can improve the heat transfer matching between the hot and cold fluids on both sides of the heat exchanger, thereby reducing the irreversibility losses in the heat transfer process, as shown in Figure 2b.

It is due to that the saturated liquid temperature of the ORC system using mixed OWM is not the same as the saturated vapor temperature during the evaporation and condensation processes, which leads to the ORC system using mixed OWM having four operational conditions due to various state locations of ET (T_{eva}) and CT (T_{con}), which are shown in Figure 3.

As shown in Figure 3, Condition 1 is that the ET and CT of the OWM correspond to the saturated liquid temperatures during the evaporation and condensation processes, respectively. Condition 2 is that the ET of OWM is the saturated vapor temperature during the evaporation process, and the CT of OWM is the saturated liquid temperature during the condensation process. Condition 3 is that the ET of OWM is the saturated liquid temperature during the evaporation process, and the CT of OWM is the saturated vapor temperature during the condensation process. Condition 4 is that the ET and CT of OWM are the saturated vapor temperatures during the evaporation and condensation processes, respectively. Furthermore, due to the effect of slip temperature of mixed OWM, the energy, exergy, and economic performances of the ORC system under four operational conditions are also entirely different for the given ORC crucial parameters.

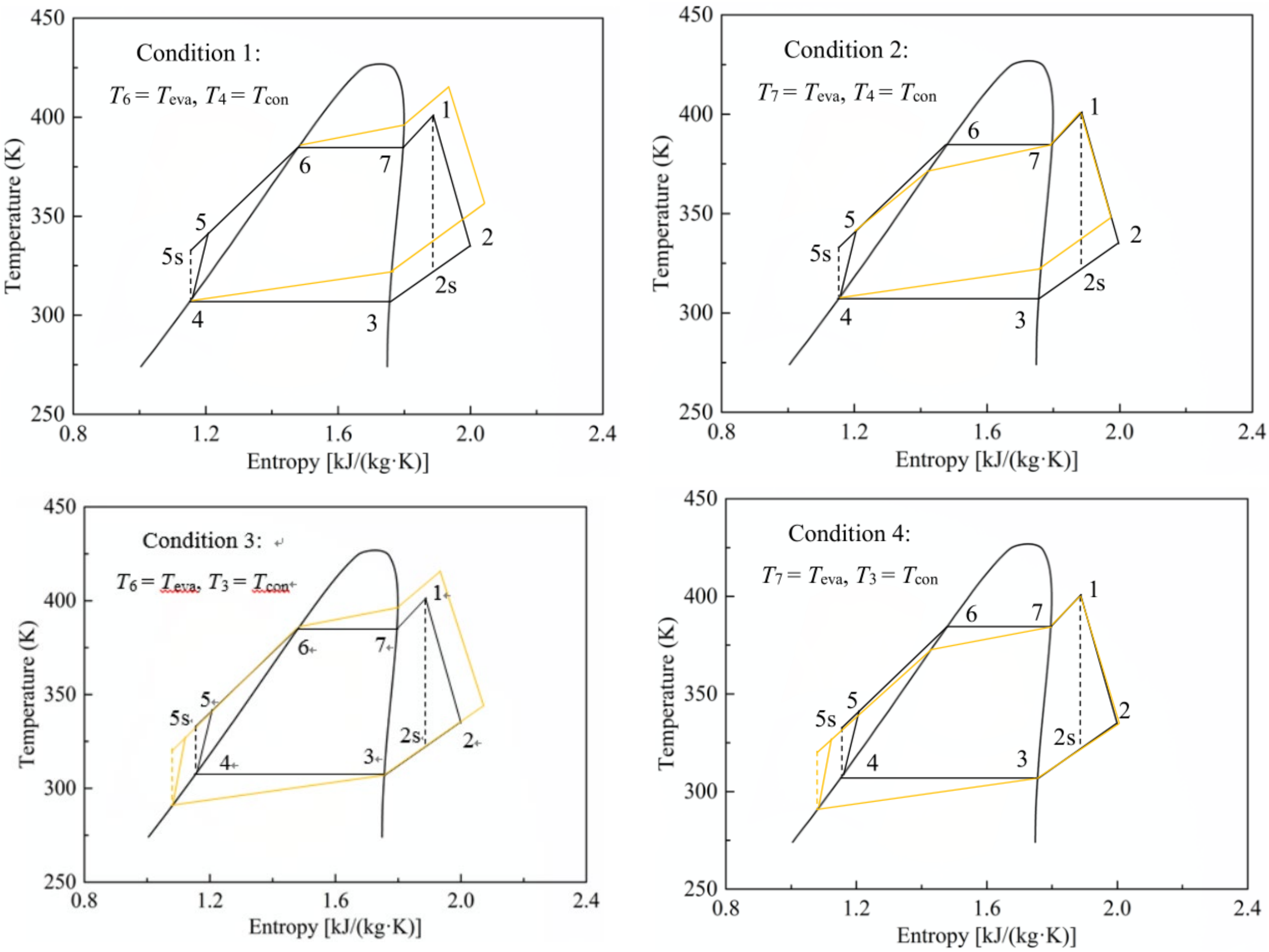

Figure 3. *T-s* diagrams of four operational conditions for the ORC system using mixed OWM.

2.2. Energy and Exergy Models

The calculation of the heat exchange quantity (Q_{eva}) in the evaporator of the ORC system utilizing both pure and mixed OWMs is presented as follows.

$$Q_{eva} = m_f(h_1 - h_5) = m_g(h_8 - h_{11}) \quad (1)$$

The practical power output in the expander (W_e) is determined below.

$$W_e = m_f(h_1 - h_2) = m_f(h_1 - h_{2s})\eta_e \quad (2)$$

where h_{2s} is the specific enthalpy of OWM at condensing pressure after isentropic expansion.

OWM releases heat to the cooling water, and the calculation of the condensing heat release of the ORC system (Q_{con}) is as follows.

$$Q_{con} = m_f(h_2 - h_4) = m_w(h_{14} - h_{12}) \quad (3)$$

The practical power consumption in the pump (W_p) is determined below.

$$W_p = m_f(h_5 - h_4) = m_f(h_{5s} - h_4)/\eta_p \quad (4)$$

where h_{4s} is the specific enthalpy of OWM at evaporating pressure after isentropic compression.

In accordance with the first and second laws of thermodynamics [41], the net power output (W_{net}) and system exergy efficiency (η_{ex}) of the ORC system can be determined below.

$$W_{\text{net}} = W_{\text{e}} - W_{\text{p}} \tag{5}$$

$$\eta_{\text{ex}} = \frac{W_{\text{net}}}{m_{\text{g}} c_{\text{g}} \left(T_8 - T_{11} - T_0 \ln \frac{T_8}{T_{11}} \right)} \times 100\% \tag{6}$$

where T_8 and T_{11} are the inlet and outlet temperatures of LFG, respectively.

2.3. Determination of Heat Exchanging Area

The total heat exchange area (THA) of the ORC system encompasses the heat exchange areas of both the evaporator and the condenser. Taking the evaporator preheating process (A_{preh}) as an example, the heat exchange area is calculated as follows [42].

$$Q_{\text{preh}} = m_{\text{f}} (h_6 - h_5) \tag{7}$$

$$\Delta T_{\text{m,preh}} = \frac{(T_{11} - T_5) - (T_{10} - T_6)}{\ln \left(\frac{T_{11} - T_5}{T_{10} - T_6} \right)} \tag{8}$$

$$A_{\text{preh}} = \frac{Q_{\text{preh}}}{U_{\text{preh}} \Delta T_{\text{m,preh}}} \tag{9}$$

where $\Delta T_{\text{m,preh}}$ is the logarithmic mean temperature difference (LMTD) in the preheating process, and U_{preh} is the overall heat transfer coefficient of OWM with the heat source.

The heat exchange area for the evaporation process and the superheating process is calculated in the same way as above.

$$A_{\text{evap}} = \frac{Q_{\text{evap}}}{U_{\text{evap}} \Delta T_{\text{m,evap}}} \tag{10}$$

$$A_{\text{suph}} = \frac{Q_{\text{suph}}}{U_{\text{suph}} \Delta T_{\text{m,suph}}} \tag{11}$$

The THA in the evaporator (A_{eva}) is determined below.

$$A_{\text{eva}} = A_{\text{preh}} + A_{\text{evap}} + A_{\text{suph}} \tag{12}$$

Based on the findings from previous literature [42,43], the total heat transfer coefficients for the preheating, evaporating, and superheating processes are shown in Table 1.

Table 1. Overall heat transfer coefficients in the evaporator and condenser.

Coefficients (W/(m^2·K))	U_{preh}	U_{evap}	U_{suph}	U_{prec}	U_{cond}
Value	170	140	90	600	900

The heat exchange areas for the precooling and condensing processes in the condenser are also calculated below.

$$A_{\text{prec}} = \frac{Q_{\text{prec}}}{U_{\text{prec}} \Delta T_{\text{m,prec}}} \tag{13}$$

$$A_{\text{cond}} = \frac{Q_{\text{cond}}}{U_{\text{cond}} \Delta T_{\text{m,cond}}} \tag{14}$$

The THA in the condenser (A_{con}) is determined below.

$$A_{\text{con}} = A_{\text{prec}} + A_{\text{cond}} \tag{15}$$

The overall heat transfer coefficients for both the precooling and condensing processes are also presented in Table 1, according to Ref. [42].

According to the above calculation results of A_{eva} and A_{con}, the THA of the ORC system (A_{tot}) is calculated below.

$$A_{tot} = A_{eva} + A_{con} \tag{16}$$

2.4. Economic Model

The electricity production cost (*EPC*) is the whole investment cost (WIC) of W_{net} of 1 kWh [44], which is one of the most important indicators of economic performance. Therefore, this study chooses to use EPC to evaluate the economic performance of the ORC system.

The WIC of the whole system includes the investment cost of the evaporator, condenser, expander, and pump, and the investment amount of each component equipment of the system is calculated as follows [45].

$$\mathrm{lg}C_{b,i} = K_1 + K_2\mathrm{lg}Z + K_3(\mathrm{lg}Z)^2 \tag{17}$$

where $C_{b,i}$ is the calculated investment cost of each component on the basis of dollar value at 1996. K_1, K_2, and K_3 represent the coefficients for each component, with their values provided in Table 2 [30,45]. Z represents the heat exchange area for the heat exchanger, the expansion power for the expander, and the power consumption for the pump.

Table 2. Cost coefficients of each system component.

Components	K_1	K_2	K_3	C_1	C_2	C_3	B_1	B_2	F_m	F_{bm}
Expander	3.514	0.589	0	/	/	/	/	/	/	3.5
Pump	3.389	−0.054	0.154	0	0	0	1.89	1.35	1.5	/
Exchanger	4.666	−0.156	0.155	0	0	0	0.96	1.21	2.45	/

Based on the material and pressure conditions of each component, the investment cost for each component must be adjusted, and the revised investment cost of each component (C_i) is calculated below.

$$\mathrm{lg}F_{p,i} = C_1 + C_2\mathrm{lg}P + C_3(\mathrm{lg}P)^2 \tag{18}$$

$$C_i = C_{b,i}F_{bm} = C_{b,i}(B_1 + B_2F_mF_{p,i}) \tag{19}$$

where $F_{p,i}$ is the pressure correction factor. C_1, C_2 and C_3 are the coefficients of each component. P is the average pressure at the inlet and outlet of the corresponding component. C_i is the corrected investment cost of each component. For the expander, F_{bm} is a constant value, while B_1, B_2, and F_m represent the coefficients for each component, with their respective values shown in Table 2 [30,45].

In conclusion, the equation for calculating the WIC ($C_{tot,1996}$) is determined below.

$$C_{tot,1996} = \sum C_i \tag{20}$$

Based on the time value of money, the WIC from 1996 needs to be adjusted to reflect the WIC of 2021, and the calculation formula for $C_{tot,2021}$ is as follows.

$$C_{tot,2021} = \frac{C_{tot,1996}CEPCI_{2021}}{CEPCI_{1996}} \tag{21}$$

where *CEPCI* is the Chemical Engineering Plant Cost Index, and the values of $CEPCI_{1996}$ and $CEPCI_{2021}$ are 382 [46] and 708 [47], respectively.

The equation for calculating the cost recovery factor (*CRF*) is provided below [30].

$$CRF = \frac{j(1+j)^{\mathrm{PL}}}{(1+j)^{\mathrm{PL}} - 1} \tag{22}$$

where j is the annual interest rate and set to be 5%, and PL is the system effective service time and set to be 20 years [48].

Therefore, the *EPC* is simplified by ignoring the field capital cost and the field O and M cost and is calculated below [44].

$$EPC = \frac{(CFR \cdot C_{\mathrm{tot,2021}} + OMC)}{t_{\mathrm{op}} \cdot W_{\mathrm{net}}} \tag{23}$$

where *OMC* represents the operation and maintenance costs of the ORC system and is set to be 1.5% of WIC in 2021, and the t_{op} represents the effective operation time of the ORC system with a setting value of 8000 h.

2.5. Bi-Objective Optimization Model

This study employs η_{ex} and *EPC* as evaluation indicators for bi-objective optimization of key ORC parameters, with the specific evaluation indices outlined below.

The first evaluation index $F_1(\eta_{\mathrm{ex}})$:

$$\text{Max: } F_1(\eta_{\mathrm{ex}}) = \eta_{\mathrm{ex}} / \eta_{\mathrm{ex,max}} \tag{24}$$

The second evaluation index $F_2(EPC)$:

$$\text{Max: } F_2(EPC) = EPC_{\mathrm{min}} / EPC \tag{25}$$

where $\eta_{\mathrm{ex,max}}$ is the largest η_{ex} in the variation range of the crucial parameter, and EPC_{min} is the smallest *EPC*.

It is important to highlight that the first and second evaluation indices mentioned above should achieve either the best or maximum value within the range of critical parameters. In this study, the bi-objective optimization model incorporating these two evaluation indices is solved using the linear weighted evaluation function approach.

The bi-objective function $F(\eta_{\mathrm{ex}}, EPC)$ is calculated below.

$$F(\eta_{\mathrm{ex}}, EPC) = \alpha F_1(\eta_{\mathrm{ex}}) + \beta F_2(EPC) \tag{26}$$

where α and β are the weighting coefficients of the above two evaluation indexes, respectively, the calculation methods of which are elaborated in the previous literature [49], and the specific equations are shown below.

$$\alpha = \left(F_2{}^1 - F_2{}^2\right) / \left[\left(F_1{}^2 - F_1{}^1\right) + \left(F_2{}^1 - F_2{}^2\right)\right] \tag{27}$$

$$\beta = \left(F_1{}^2 - F_1{}^1\right) / \left[\left(F_1{}^2 - F_1{}^1\right) + \left(F_2{}^1 - F_2{}^2\right)\right] \tag{28}$$

where $F_1{}^1$ is the minimum value of $F_1(\eta_{\mathrm{ex}})$, $F_1{}^2$ is the value of $F_1(\eta_{\mathrm{ex}})$ when the value of $F_2(EPC)$ is minimized, $F_2{}^2$ is the minimum value of $F_2(EPC)$, and $F_2{}^1$ is the value of $F_2(EPC)$ when the value of $F_1(\eta_{\mathrm{ex}})$ is minimized.

2.6. Selection of Mixed OWM

Choosing the appropriate OWM can effectively enhance the power generation efficiency of the ORC system and reduce operational costs, making the selection of OWM crucial. According to the selection criteria for OWM [14], the research findings suggest that both isobutane (R600a) and isopentane (R601a) are classified as dry OWM and can deliver superior system performance compared to other options when evaluated based on thermal, economic, and environmental criteria [41,50]. Therefore, according to the temperature characteristics of LFG, this study selects R600a, R601a, and their mixtures in different proportions as the OWMs for the ORC system. Table 3 presents the physical property parameters of R600a and R601a, while Table 4 displays the corresponding parameters of the mixed OWM (M_{R600a}) at different mass fractions of R600a. Figure 4 displays the *T-s* diagrams for R600a, R601a, and their mixtures, derived from the relationship between temperature and entropy of the OWM.

Table 3. Physical property parameters of R600a and R601a.

Substance	Isobutane (R600a)	Isopentane (R601a)
Type	Dry	Dry
Molar mass (g/mol)	58.12	72.15
Boiling point temperature (K)	261.41	300.98
Critical temperature (K)	407.85	460.35
Critical pressure (MPa)	3.63	3.378
Ozone depletion potential	0	0
Global warming potential	20	4

Table 4. Related parameters of mixed OWM under various M_{R600a}.

M_{R600a}	Molar Mass (g/mol)	Critical Temperature (K)	Critical Pressure (MPa)
0.1	70.45	455.6	3.491
0.2	68.83	450.7	3.583
0.3	67.28	445.67	3.654
0.4	65.8	440.51	3.705
0.5	64.38	435.27	3.738
0.6	63.02	429.94	3.752
0.7	61.72	424.54	3.749
0.8	60.47	419.07	3.728
0.9	59.28	413.5	3.689

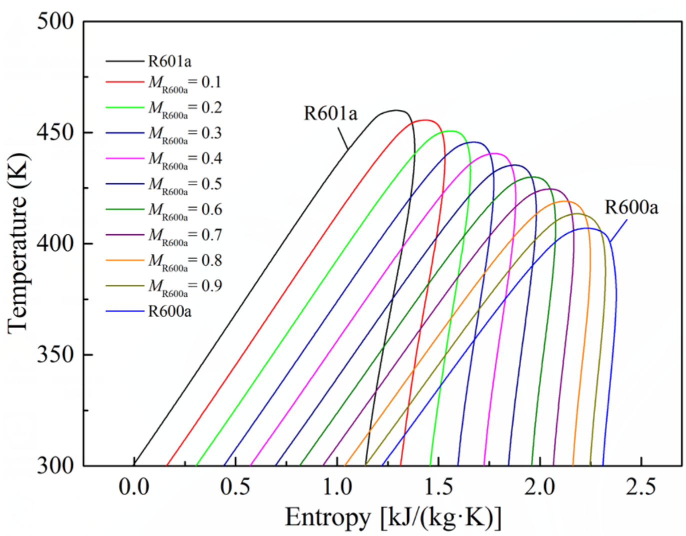

Figure 4. *T-s* diagrams of R600a, R601a, and their mixtures.

2.7. Model Validation

To verify the accuracy of the calculation model used in this paper, the calculated results of the ORC system using R600, R601a, and their different mixture ratios are compared with the results from the literature [51], as shown in Table 5. The W_{net} and cycle thermal efficiency (η_{cycle}) are selected as the comparative performance index, and the calculation equation of η_{cycle} is determined below.

$$\eta_{cycle} = \frac{W_{net}}{Q_{eva}} \times 100\% \quad (29)$$

Table 5. Comparison between current study and Ref. [51].

M_{R601a}	W_{net} in Ref. [51]/kW	W_{net} in Current Study/kW	Relative Deviation/%	η_{cycle} in Ref. [51]	η_{cycle} in Current Study	Relative Deviation/%
0	34.69	34.57	0.35	11.15	11.13	0.18
0.1	34.19	34.08	0.32	11.03	11	0.27
0.2	33.74	33.61	0.39	10.92	10.89	0.27
0.3	33.35	33.25	0.3	10.82	10.8	0.18
0.4	33.03	32.89	0.42	10.73	10.71	0.19
0.5	32.79	32.67	0.37	10.68	10.66	0.19
0.6	32.65	32.51	0.43	10.64	10.61	0.28
0.7	32.64	32.53	0.34	10.65	10.62	0.28
0.8	32.82	32.71	0.34	10.7	10.68	0.19
0.9	33.26	33.17	0.27	10.83	10.81	0.18
1.0	34.1	33.98	0.35	11.06	11.04	0.18

As can be seen from Table 5, the calculated results of W_{net} and η_{cycle} under different mass fractions of R601a in the mixed OWM are generally consistent with the findings in the literature [51], with relative errors all being less than 0.5%. Therefore, the comparison results validate the feasibility and reliability of the calculation model established in this paper.

3. Results and Discussion

In the current study, the calculations for the energy, exergy, and economic models mentioned above are conducted using Matlab and Refprop software. The M_{R600a} and ORC crucial parameters, including the ET, CT, and SD of OWM, are set as the variable parameters, and the changes of W_{net}, η_{ex}, system THA and *EPC* with the M_{R600a}, ET, CT, and SD of OWM under four operational conditions are investigated in detail. Then, the contrastive analysis of energy, exergy, and economic performances under four operational conditions are also conducted. Finally, the M_{R600a}, ET, CT, and SD of OWM under four operational conditions are separately optimized by taking the η_{ex} and *EPC* as the evaluation indexes of parameter optimization. The initial calculation parameters for the ORC system using pure OWM and mixed OWM are shown in Table 6. Taking into account the slip temperature of mixed OWM, as well as the inlet temperatures of the heat source and heat sink, Table 7 lists the upper and lower limit settings for the four variable parameters.

Table 6. Initial parameters of ORC system.

Parameters	m_g (kg/s)	T_8 (K)	T_{12} (K)	η_p (%)	η_e (%)	$\Delta T_{6\text{-}10}$ (K)	$\Delta T_{3\text{-}13}$ (K)	T_0 (K)
Value	180	433.15	293.15	80	85	10	5	293.15

Table 7. Lower and upper bounds for four variable parameters.

Variable Parameters	Lower Bound	Upper Bound
M_{R600a}	0	1
T_{eva} (K)	363.15	393.15
T_{con} (K)	308.15	323.15
ΔT_{sup} (K)	0	15

3.1. Effect of Mass Fraction on System Performance

The M_{R600a} has a significant impact on the physical performance parameters of mixed OWM, as illustrated in Table 3 and Figure 4. When the ET, CT, and SD of OWM are 383.15 K, 313.15 K, and 10 K, respectively, the change of slip temperature with the M_{R600a} under various state locations of ET and CT is displayed in Figure 5. Figure 5 shows that the slip temperatures of mixed OWM during both the evaporation and condensation processes first rise and then reduce as the M_{R600a} rises, and when the M_{R600a} is 0.3, the slip temperature of mixed OWM reaches the maximum value under various conditions. Furthermore, the slip temperatures of mixed OWM under various state locations of ET and CT are also different, and when the saturated vapor temperatures during the evaporation and condensation processes are set as the ET and CT, the slip temperatures of mixed OWM are relatively larger. Moreover, the slip temperature of mixed OWM during the condensation process is greater than that during the evaporation process for a fixed M_{R600a}.

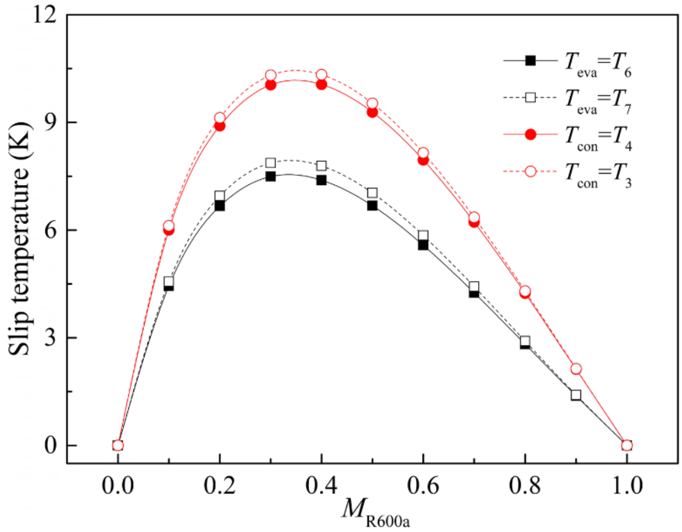

Figure 5. Change of slip temperature with M_{R600a} under various state locations of ET and CT.

Based on the specified values of the variable parameters mentioned above, the changes of W_{net} and η_{ex} with the M_{R600a} under four operational conditions are displayed in Figure 6. As seen in Figure 6, the W_{net} and η_{ex} under four operational conditions vary greatly with rising M_{R600a}, and the W_{net} and η_{ex} of condition 3 and condition 4 first rise and then reduce, while the W_{net} and η_{ex} of condition 1 and condition 2 first reduce and then rise. Furthermore, compared with the pure OWM, the ORC system of condition 4 using the mixed OWM can achieve the larger W_{net} in four operational conditions, while the η_{ex} of the mixed OWM in condition 3 is relatively larger. This is attributed to the fact that, when the saturated liquid temperatures during the evaporation and condensation processes are set as the ET and CT, both the m_f and W_{net} per unit m_f first reduce and then rise as the M_{R600a} rises due to the existence of slip temperature. On the contrary, the m_f and W_{net} per unit m_f first rise and then reduce when the saturated vapor temperatures during the evaporation and condensation processes are set as the ET and CT. However, the variation amplitude of W_{net} per unit m_f is larger than that of m_f under four operational conditions, so the W_{net} of four operational conditions occurs in the above variation trend. Moreover, the variations of m_f under four operational conditions makes it so that the heat source outlet temperatures (T_{11}) of condition 1 and condition 3 steadily reduce as the M_{R600a} rises based on the first law of thermodynamics in the preheating process, while the T_{11} of condition 2 and condition 4 first reduce and then rise, and the T_{11} of condition 1 and condition 3 are greater than that of condition 2 and condition 4 for a fixed M_{R600a}. It is due to the fact that the variation amplitudes of T_{11} in the range of M_{R600a} under four operational conditions are relatively smaller, which leads to the fact that the variation trend of η_{ex} is the same as that of W_{net} for a given operational condition based on Equation (6).

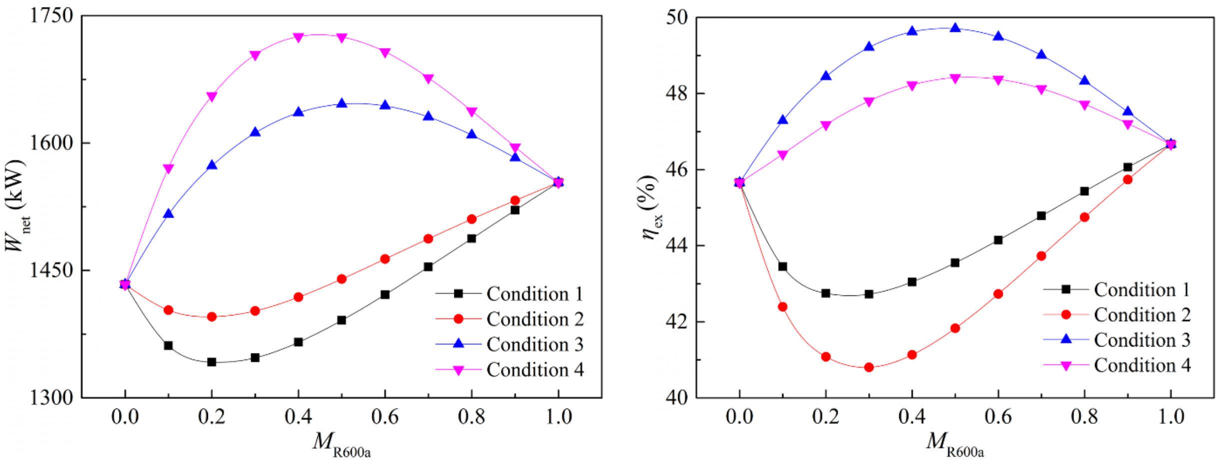

(**a**) W_{net} (**b**) η_{ex}

Figure 6. Changes of W_{net} and η_{ex} with M_{R600a}.

As also seen in Figure 6, the W_{net} of condition 4 and the η_{ex} of condition 3 are the maximum in four operational conditions for a fixed M_{R600a}, while the W_{net} of condition 1 and the η_{ex} of condition 2 are the minimum. This is attributed to the fact that, when the saturated vapor temperature during the evaporation process is set as the ET of OWM for condition 2 and condition 4, the heat source temperature drop during the evaporation process becomes larger accordingly due to the existence of slip temperature by comparing with the other conditions, and the Q_{eva} also becomes larger, which leads to the ORC system being able to achieve the larger m_f and lower T_{11}. Meanwhile, when the saturated liquid temperature during the condensation process is set as the CT of OWM for condition 1 and condition 2, the specific enthalpy of OWM at the expander outlet is relatively larger due to the existence of slip temperature during the condensation process, so the ORC system can achieve the smaller W_{net} per unit m_f. Compared with condition 3, condition 4 has the larger m_f and the smaller W_{net} per unit m_f, and it is due to the fact that the specific value of W_{net} per unit m_f is greater than that of m_f in four operational conditions, so the W_{net} of condition 4 is relatively larger. In a similar way, the condition 1 has the smaller m_f and the larger W_{net} per unit m_f by comparing with condition 2, so the W_{net} of condition 1 is relatively smaller. Furthermore, it is due to the fact that the T_{11} of conditions 2 and 4 are separately less than that of conditions 1 and 3 for a fixed M_{R600a}, which leads to the heat source exergy drops in the evaporator of conditions 2 and 4 being separately greater than that of conditions 1 and 3, so the η_{ex} of conditions 2 and 4 are separately less than that of conditions 1 and 3 based on Equation (6). Moreover, the W_{net} of condition 4 with the M_{R600a} of 0.4 reaches the maximum value, which is 11% higher than the W_{net} of R600a, and the η_{ex} of condition 3 with the M_{R600a} of 0.5 also reaches the maximum value, which is 8.8% higher than the η_{ex} of R601a, showing the better energy and exergy performances.

Figure 7 shows the changes of system THA and *EPC* with the M_{R600a}. As seen in Figure 7a, the system THA of condition 1 steadily rises with rising M_{R600a}, while the system THA of the other three conditions first rises and then reduces. This is attributed to the fact that, when the saturated liquid temperature during the condensation process is set as the CT of OWM for condition 1 and condition 2, the LMTD in the condenser changes a little with the rise of M_{R600a} due to the fixed $\Delta T_{3\text{-}13}$. In condition 1, the rise of M_{R600a} makes the rise of m_f and reduction of T_{11}, the Q_{eva} and Q_{con} also rise accordingly, and the LMTD in the evaporator steadily reduces, which leads to the rise of system THA. In condition 2, the m_f first rises and then reduces with rising M_{R600a}, while the T_{11} first reduces and then rises as the M_{R600a} rises, so both the Q_{eva} and Q_{con} first rise and then reduce. Furthermore, the

LMTD in the condenser also changes marginally due to the fixed $\Delta T_{6\text{-}10}$, which leads to the THA of condition 2 first rising and then reducing. Moreover, when the saturated vapor temperature during the condensation process is set as the CT of OWM for condition 3 and condition 4, the LMTD in the condenser first reduces and then rises with the rise of M_{R600a} due to the existence of slip temperature. In condition 3, the change of m_f is the same as that in condition 1, and the T_{11} also reduces as the M_{R600a} rises, which leads to the rise of Q_{eva} and Q_{con} and reduction of LMTD in the evaporator, so the system THA also first rises and then reduces with rising M_{R600a}. In condition 4, the change trends of m_f, T_{11}, Q_{eva}, and Q_{con} are the same as those in condition 2, and the LMTD in the condenser also changes a little due to the fixed $\Delta T_{6\text{-}10}$, so the system THA also first rises and then reduces.

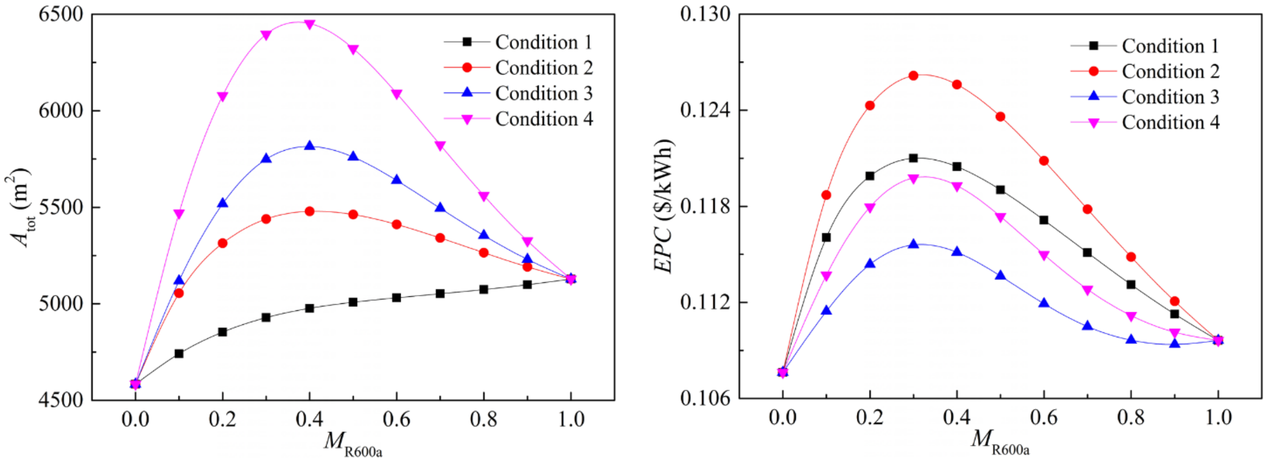

(**a**) system THA (**b**) *EPC*

Figure 7. Changes of system THA and *EPC* with M_{R600a}.

As also seen in Figure 7a, the system THA of condition 4 is the maximum in four operational conditions for a fixed M_{R600a}, while the system THA of condition 1 is the minimum. This is attributed to the fact that, when the M_{R600a} is constant, the m_f of conditions 2 and 4 are greater than that of conditions 1 and 3, and it is due to that the T_{11} of conditions 1 and 4 are the highest and the lowest in the four operational conditions, respectively, so conditions 1 and 4 have the smallest Q_{eva} and the largest Q_{con}, which leads to the maximum system THA for condition 4 and the minimum system THA for condition 1. Furthermore, although the T_{11} of condition 2 is lower than that of condition 3, the Q_{eva} and Q_{con} of condition 2 are also greater than that of condition 3. However, due to the lower LMTDs in the evaporator and condenser, the system THA of condition 3 is greater than that of condition 2.

It can be concluded in Figure 7b that the *EPC* first rises and then reduces with the rising of the M_{R600a} for a given condition. This is attributed to the fact that the larger the system THA is, the greater the WIC is. In condition 3 and condition 4, the rise amplitude of WIC shown in Figure 7a is greater than that of W_{net} shown in Figure 6a at the smaller M_{R600a}, while the reduction amplitude of WIC is also greater than that of W_{net} at the larger M_{R600a}, which leads to the *EPC* first rising and then reducing. Moreover, the WIC of condition 2 also first rises and then reduces with rising M_{R600a} based on the variation of system THA shown in Figure 7a, and it is due to the fact that the variation trend of W_{net} is in the opposite direction to that of WIC, so the *EPC* of condition 2 first rises and then reduces as the M_{R600a} rises. In condition 1, the W_{net} first reduces and then rises with rising M_{R600a}, and the rise amplitude of WIC is less than that of W_{net} at the larger M_{R600a}, so the *EPC* first rises and then reduces.

As also seen in Figure 7b, the *EPC* of condition 2 is the maximum in four operational conditions for a fixed M_{R600a}, while the *EPC* of condition 3 is the minimum. Furthermore, the *EPC* of mixed OWM is greater than that of pure OWM for a fixed operational condition, and when the M_{R600a} is 0.4, the *EPC* is the maximum in four operational conditions. Moreover, the R601a has the smallest *EPC* in the variation range of the M_{R600a}, which is 1.8% lower than the *EPC* of the R600a, showing the better economic performance.

3.2. Effect of ET on System Performance

When the M_{R600a}, CT, and SD of OWM are 0.6, 313.15 K, and 10 K, respectively, the change of slip temperature with the ET of OWM under various state locations of ET is displayed in Figure 8. As concluded from Figure 8, the slip temperature of mixed OWM steadily reduces with rising the ET of OWM, and the slip temperature at the saturated vapor temperature is greater than that at the saturated liquid temperature for a fixed ET of OWM, while the reduction amplitude of slip temperature at the saturated vapor temperature is basically the same as that at the saturated liquid temperature. Moreover, as the ET of OWM rises by 2 K, the slip temperature reduces the average of 0.09 K.

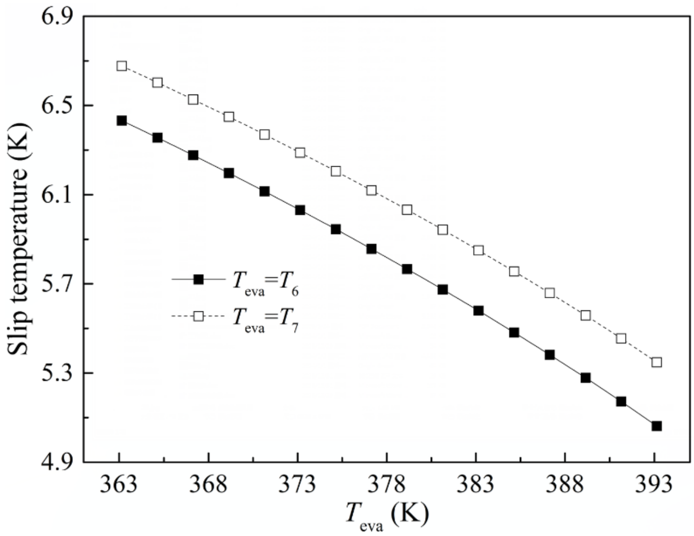

Figure 8. Change of slip temperature with ET of OWM.

Figure 9 shows the changes of W_{net} and η_{ex} with the ET of OWM. As concluded from Figure 9, the W_{net} first rises and then reduces with raising the ET of the OWM for a certain condition, while the η_{ex} steadily rises. This can be attributed to the rise in the ET of OWM, which causes T_{11} to increase, while both Q_{eva} and m_f decrease accordingly. Meanwhile, raising the ET of OWM also makes the specific enthalpy of OWM at the evaporator outlet the W_{net} per unit m_f, and this steadily rises. When the ET of OWM is lower, the increase in W_{net} per unit of m_f is greater than the decrease in m_f, so it can be seen from Equation (5) that W_{net} increases steadily. However, the reduction amplitude of m_f gradually becomes larger with raising the ET of OWM, which is greater than the rise amplitude of W_{net} per unit m_f when the ET of OWM is higher, so the W_{net} steadily reduces. Furthermore, it is due to that the T_{11} rises with raising the ET of OWM, which leads to the denominator value in Equation (6) reducing accordingly, and the reduction amplitude of the denominator value in Equation (6) is larger than that of W_{net} when the ET of OWM is higher, so the η_{ex} rises based on Equation (6).

As seen in Figure 9, when the ET of OWM is lower than 371.15 K, the W_{net} of condition 3 is the maximum in four operational conditions for a given ET of OWM, while the W_{net} of condition 2 is the minimum. When the ET of OWM is lower than 375.15 K, condition 4 and condition 1 can achieve the maximum and minimum W_{net}, respectively. Furthermore, the η_{ex} of condition 3 is the maximum in four conditions with the rise of ET of OWM, while the η_{ex} of condition 2 is the minimum, which are consistent with the results in Figure 6b. Compared with the other two conditions, condition 3 and condition 4 can achieve better energy and exergy performances in the variation range of ET of OWM.

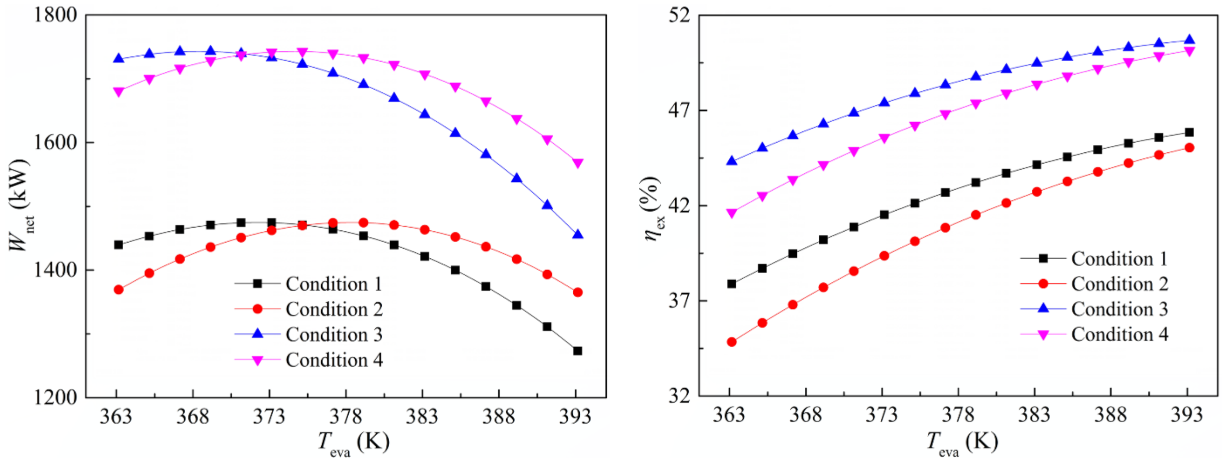

(**a**) W_{net} (**b**) η_{ex}

Figure 9. Changes of W_{net} and η_{ex} with ET of OWM.

Figure 10 shows the changes of system THA and *EPC* with the ET of OWM. As concluded from Figure 10, both the system THA and *EPC* steadily reduce with raising the ET of OWM for a certain condition. This is attributed to the fact that raising the ET of OWM makes the reduction of Q_{eva} and m_f, and the Q_{con} also reduces, which leads to the THA reducing accordingly. Furthermore, the reduction of system THA also makes the reduction of WIC, and the reduction amplitude of WIC is larger than that of W_{net} when the ET of OWM is higher, so the *EPC* reduces as the ET of OWM rises based on Equation (23). Moreover, the reduction amplitude of WIC basically remains unchanged with raising the ET of OWM, while the reduction amplitude of W_{net} gradually becomes larger, which leads to the smaller reduction amplitude of *EPC* at the higher ET of OWM.

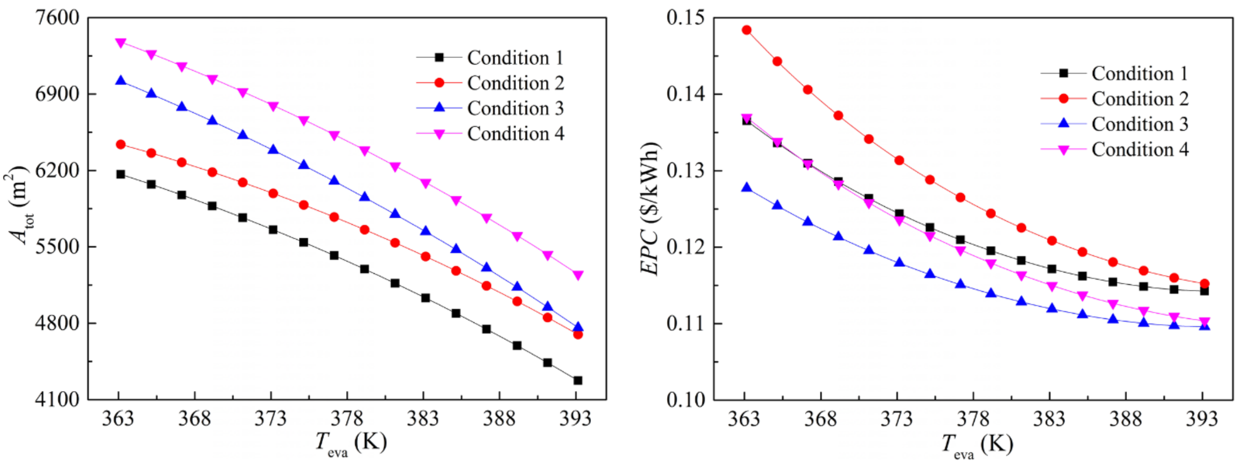

(**a**) system THA (**b**) *EPC*

Figure 10. Changes of system THA and *EPC* with ET of OWM.

As also seen in Figure 10, the system THA of condition 4 and the *EPC* of condition 2 are the maximum in four operational conditions for a fixed ET of OWM, while the system THA of condition 1 and *EPC* of condition 3 are the minimum, which are consistent with the results in Figure 7. The above results mean that compared with the other three conditions, condition 3 can achieve better economic performance in the variation range of ET of OWM.

3.3. Effect of CT on System Performance

When the M_{R600a}, ET, and SD of OWM are 0.6, 383.15 K, and 10 K, respectively, the change of slip temperature with the CT of OWM under various state locations of CT is displayed in Figure 11. As concluded from Figure 11, the higher the CT of the OWM is, the smaller the slip temperature of mixed OWM during the condensation process is, and when the CT of OWM is set as the saturated liquid temperature, the slip temperature of mixed OWM is relatively smaller for a fixed CT of OWM. Furthermore, as the CT of OWM rises by 2 K, the slip temperature reduces the average of 0.05 K.

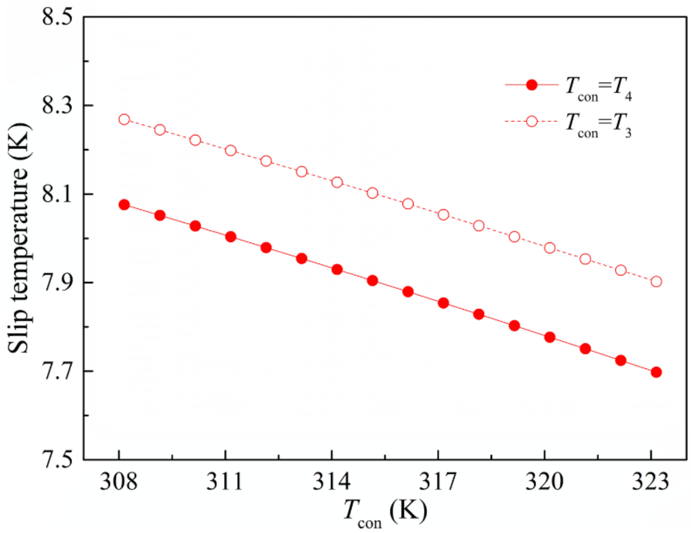

Figure 11. Change of slip temperature with CT of OWM.

Figure 12 shows the changes of W_{net} and η_{ex} with the CT of OWM. As concluded from Figure 12, both the W_{net} and η_{ex} steadily reduce with raising the CT of OWM for a certain condition. This is attributed to the fact that raising the CT of OWM makes the rise of specific enthalpy of OWM at the expander outlet and has no effect on the variation of m_f, which leads to the fact that the W_{net} per unit m_f reduces, so the W_{net} also reduces accordingly. Moreover, raising the CT of OWM also makes the rise of specific enthalpy of OWM at the pump outlet, which leads to the rise of T_{11} and the reduction of heat exchanging quantity in the preheating process; the denominator value in Equation (6) reduces accordingly. However, the reduction amplitude of W_{net} is greater than that of the denominator value in Equation (6), so the η_{ex} also steadily reduces. Furthermore, the W_{net} of condition 4 and η_{ex} of condition 3 are the largest in the variation range of CT, while the W_{net} of condition 1 and η_{ex} of condition 2 are the smallest, which are consistent with the results in Figure 6. As the CT of OWM rises by 1 K, the W_{net} of condition 4 and η_{ex} of condition 3 reduce the average of 31 kW and 0.67%, respectively.

Figure 13 shows the changes of system THA and *EPC* with the CT of OWM. As concluded from Figure 13a, the system THA reduces with rising the CT of OWM for a certain condition, and the reduction amplitudes of system THA in condition 3 and in condition 4 are relatively larger. This is attributed to the fact that raising the CT of OWM makes the rise of T_{11} and the reduction of specific latent heat of OWM, as well as the rise of LMTD in the condenser, which leads to both the Q_{eva} and Q_{con} reducing due to the constant m_f, so the system THA reduces. Furthermore, when the saturated vapor temperature during the condensation process is set as the CT of OWM for condition 3 and condition 4, the rise amplitude of LMTD in the condensing section gradually becomes smaller as the CT of OWM rises due to the existence of slip temperature, which leads to the reduction amplitudes of system THA in condition 3 and in condition 4 being greater those that in condition 1 and in condition 2.

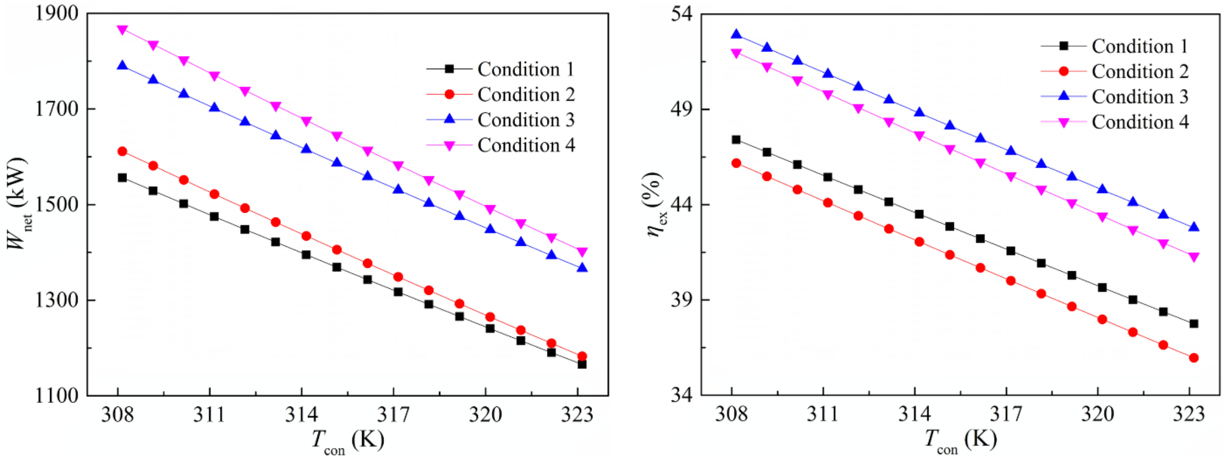

(**a**) W_{net} (**b**) η_{ex}

Figure 12. Changes of W_{net} and η_{ex} with CT of OWM.

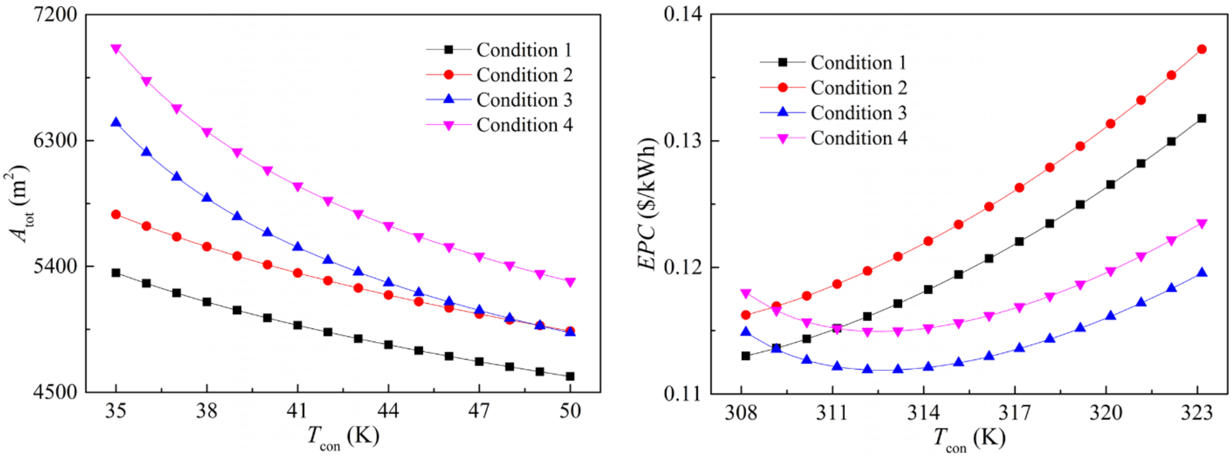

(**a**) system THA (**b**) *EPC*

Figure 13. Changes of system THA and *EPC* with CT of OWM.

As seen in Figure 13b, the *EPC*s of condition 1 and in condition 2 steadily rise with raising the CT of OWM, while the *EPC*s of condition 3 and in condition 4 first reduce and then rise. This is attributed to the fact that the reduction of system THA also makes the reduction of WIC. In condition 1 and in condition 2, the reduction amplitude of WIC is less than that of W_{net} in the variation range of CT, so the *EPC* steadily rises as the CT of OWM rises based on Equation (23). In condition 3 and in condition 4, due to the larger reduction amplitude of system THA at the lower CT of OWM, the reduction amplitude of WIC is greater than that of W_{net} with raising the CT of OWM, which leads to the reduction of *EPC*. However, when the CT of OWM is higher, the reduction amplitude of WIC gradually becomes smaller, which is less than that of W_{net} with raising the CT of OWM, so the *EPC* steadily rises. Moreover, when the CT of OWM is lower than 309.15 K, condition 1 can achieve the minimum *EPC* in four operational conditions, and on the contrary, the *EPC* of condition 3 is the smallest.

3.4. Effect of SD on System Performance

The SD of OWM has no effect on the slip temperature of mixed OWM. When the M_{R600a}, ET, and CT of OWM are 0.6, 383.15 K, and 313.15 K, respectively, the changes of W_{net} and η_{ex} with the SD of OWM are displayed in Figure 14. As concluded from Figure 14, both the W_{net} and η_{ex} reduces as the SD of OWM rises for a certain condition. This is attributed to the fact that, rising the SD of OWM makes the rise of specific enthalpy of

OWM at the evaporator outlet, the W_{net} per unit m_f also rises accordingly. It is due to that the heat source temperature drops during the evaporation process and the superheating process remains unchanged, the m_f steadily reduces with rising the SD of OWM based on the energy conservation law, and the reduction amplitude of m_f is greater than the rise amplitude of W_{net} per unit m_f, so the W_{net} steadily reduces. Furthermore, the specific enthalpy of OWM at the evaporator inlet also remains unchanged in the variation range of SD; the reduction of m_f makes the reduction of heat exchanging quantity in the preheating process, which leads to the rise of T_{11} as the SD of OWM rises, and the denominator value in Equation (6) reduces accordingly. However, the reduction amplitude of W_{net} is greater than that of the denominator value in Equation (6), so the η_{ex} steadily reduces. Moreover, when the SD of OWM is constant, condition 4 and condition 3 also achieve the maximum W_{net} and η_{ex} in four operational conditions, respectively, which are consistent with the results in Figures 6 and 12.

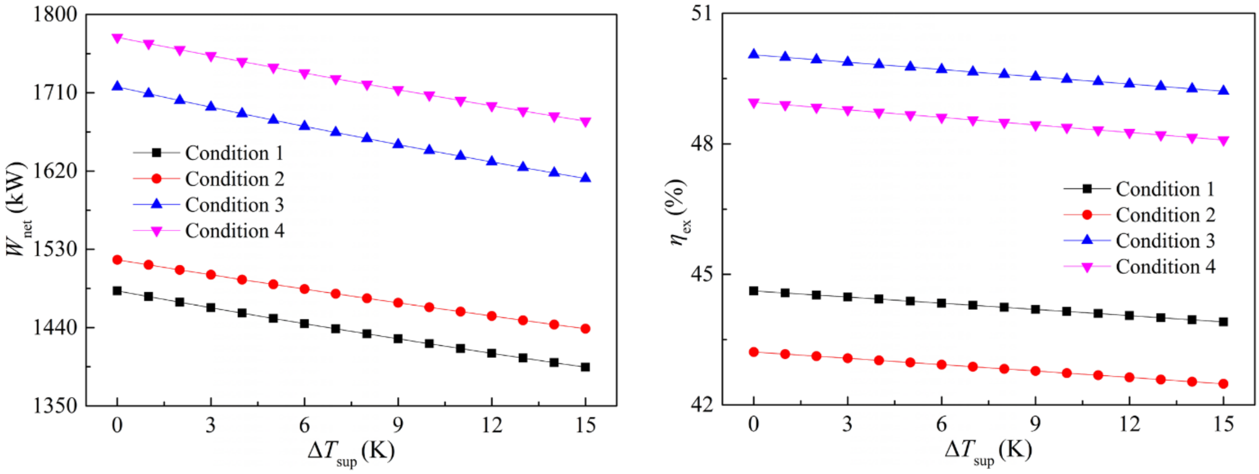

(**a**) W_{net} (**b**) η_{ex}

Figure 14. Changes of W_{net} and η_{ex} with SD of OWM.

Figure 15 shows the changes of system THA and *EPC* with the SD of OWM. As concluded from Figure 15a, the system THA reduces with rising the SD of OWM for a certain condition. This is attributed to the fact that the rise of SD makes the reduction of m_f and the rise of T_{11}, the Q_{eva} and Q_{con} steadily reduces accordingly, and it is due to that the LMTDs in the evaporator and condenser change a little with raising the SD of OWM, so the system THA also steadily reduces. Furthermore, condition 1 has the smallest system THA in four operational conditions for a fixed SD of OWM, and as the SD of OWM rises by 1 K, the system THA of condition 1 reduces the average of 16.4 m^2.

As concluded from Figure 15b, the *EPC* of condition 1 rises as the SD of OWM rises, while the *EPC*s of the other three conditions first reduce and then rise. This is attributed to the fact that the reduction of system THA also makes the reduction of WIC. In condition 1, the reduction amplitude of WIC is less than that of W_{net} in the variation range of SD, so the *EPC* steadily rises. For the other three conditions, the reduction amplitude of WIC is greater than that of W_{net} when the SD is lower, so there is a situation of reducing instead of rising for the *EPC* with rising the SD of OWM. Moreover, when the SD of OWM is constant, the *EPC* of condition 2 is also the largest in four operational conditions, while the *EPC* of condition 3 is the smallest, which are consistent with the results in Figures 7 and 10.

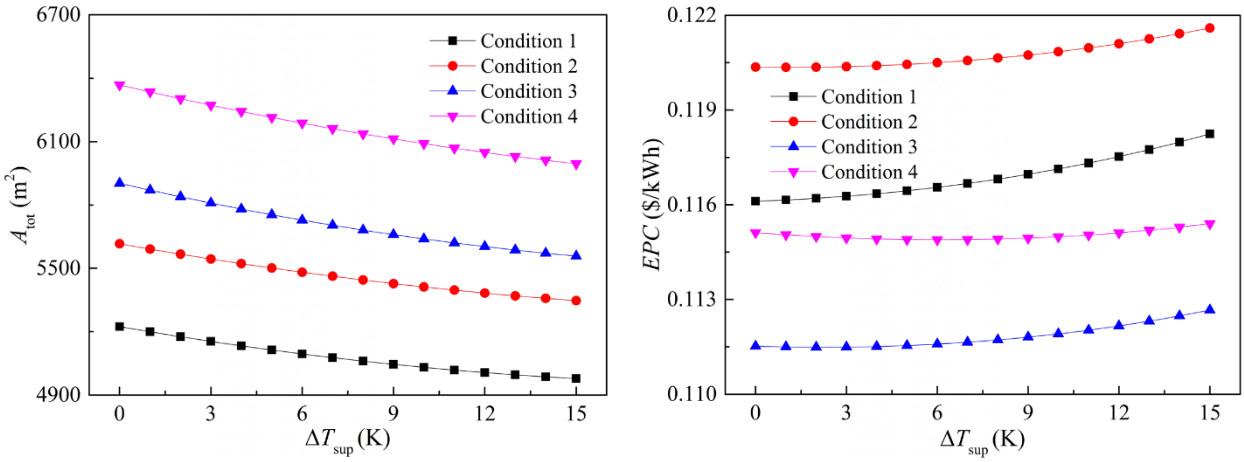

(**a**) system THA (**b**) *EPC*

Figure 15. Changes of system THA and *EPC* with SD of OWM.

3.5. Bi-Objective Optimization Analysis

In the current study, the linear weighted evaluation function method is utilized for bi-objective optimization to determine the optimal M_{R600a} among the key parameters of the mixed OWM and ORC across four operational conditions, using η_{ex} and *EPC* as the selected evaluation indices for parameter optimization.

Based on the results of η_{ex} and *EPC* shown in the above figures, the change of $F(\eta_{ex}, EPC)$ calculated through Equation (26) with the M_{R600a} under four operational conditions is displayed in Figure 16. As demonstrated in Figure 16, the change trends of $F(\eta_{ex}, EPC)$ for condition 1 and condition 2 are different from that for condition 3 and condition 4, and the $F(\eta_{ex}, EPC)$ can achieve the maximum value for a certain condition in the variation range of M_{R600a}. Based on the result analysis of Figure 16, when the M_{R600a} in mixed OWM is 0.7, the $F(\eta_{ex}, EPC)$ of condition 3 and condition 4 reach the maximum value, while the $F(\eta_{ex}, EPC)$ of condition 1 and condition 2 using the pure OWM of R600a also reach the maximum value, which denotes that the OWMs required to achieve the system's better overall performance under four operational conditions are also different.

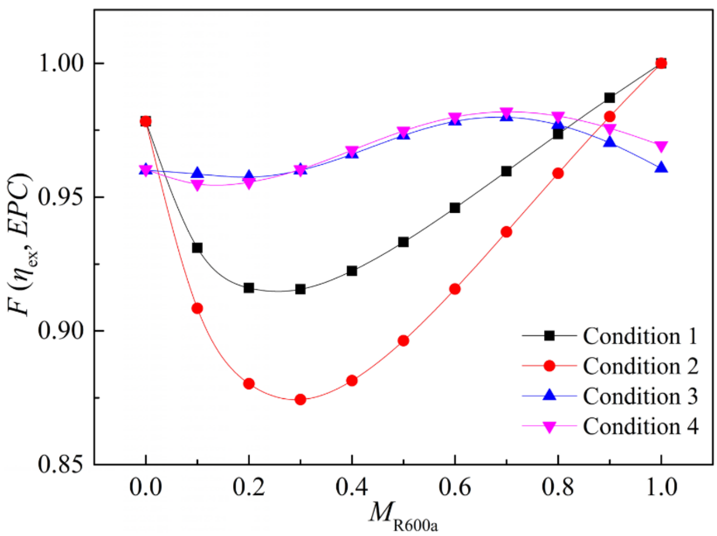

Figure 16. Change of $F(\eta_{ex}, EPC)$ with M_{R600a}.

Figure 17 shows the changes of $F(\eta_{ex}, EPC)$ with ORC crucial parameters under four operational conditions when the M_{R600a} is 0.6. As shown in Figure 17, the $F(\eta_{ex}, EPC)$ steadily rises with the rise of ET of OWM for a certain condition and reduces with the rise of CT and SD of OWM, which denotes that the higher the ET of OWM is, and the lower the CT and SD of OWM are, the better the overall performance of the ORC system is. Based on the result analysis of Figure 17, when the ET and CT of OWM are 393.15 K and 308.15 K, respectively, and the state of OWM at the evaporator outlet is the saturated vapor, the $F(\eta_{ex}, EPC)$ under four operational conditions can reach the maximum value, which denotes that the ORC crucial parameters required to achieve the better overall performance under four operational conditions are the same.

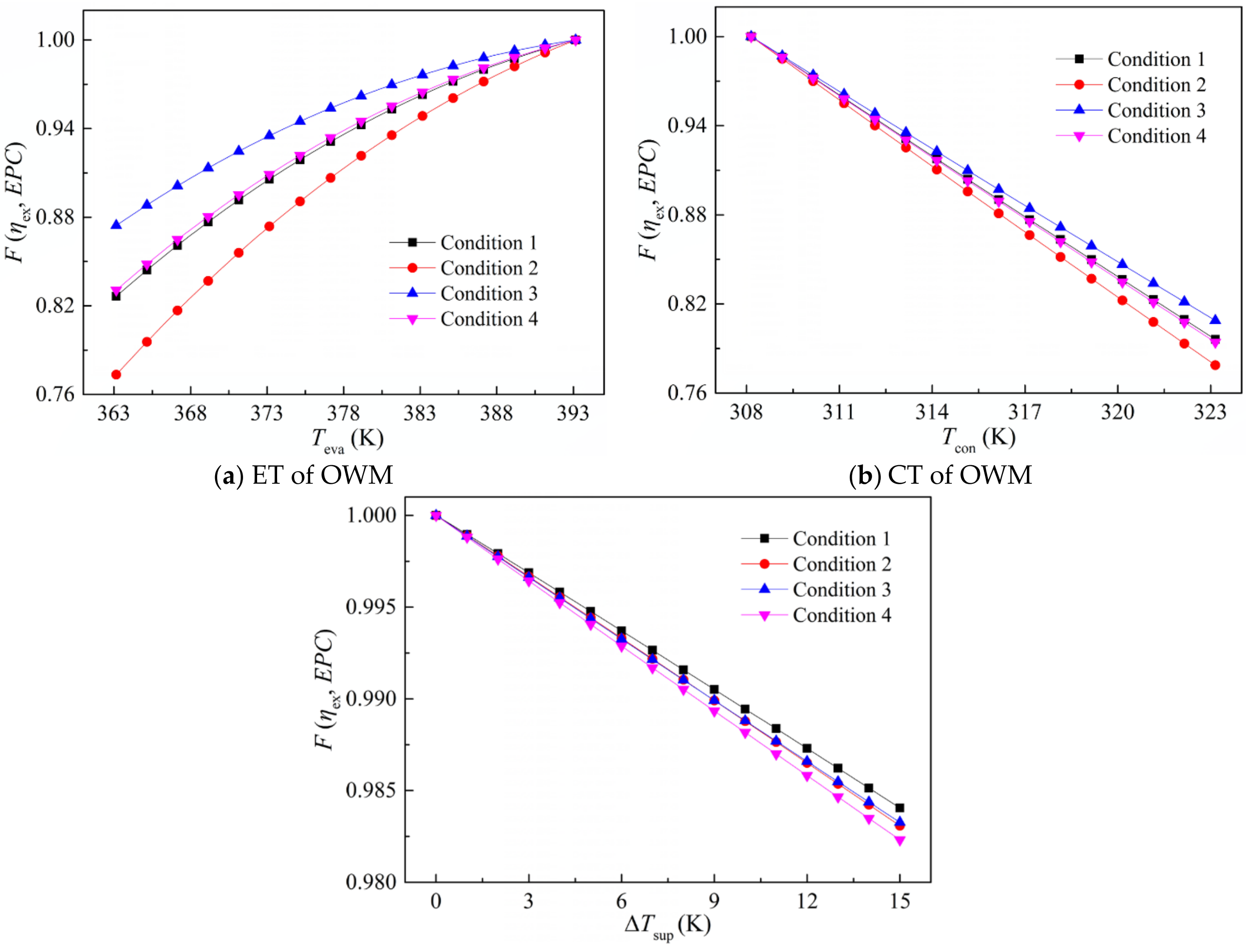

(**a**) ET of OWM (**b**) CT of OWM (**c**) SD of OWM

Figure 17. Changes of $F(\eta_{ex}, EPC)$ with ORC crucial parameters.

As known from the above results, the initial values of M_{R600a} and ORC crucial parameters under four operational conditions are not the same as the optimal values obtained from Figures 16 and 17, and to verify the reliability of the above optimal values, the M_{R600a} is reset as the variable parameter to calculate the $F(\eta_{ex}, EPC)$ under four operational conditions when the ET, CT, and SD of OWM are set to be the optimal values mentioned above, and the calculation result of $F(\eta_{ex}, EPC)$ under various M_{R600a} for four operational conditions is displayed in Figure 18. As concluded from Figure 18, the $F(\eta_{ex}, EPC)$ of condition 3 and condition 4 still reach the maximum value when the M_{R600a} are 0.7, and the $F(\eta_{ex}, EPC)$ of condition 1 and condition 2 using the pure OWM of R600a also reach the maximum value. Moreover, the specific values of T_{11}, W_{net}, η_{ex}, system THA, and *EPC* under the above optimal M_{R600a} and ORC crucial parameters for four operational conditions are summarized in Table 8.

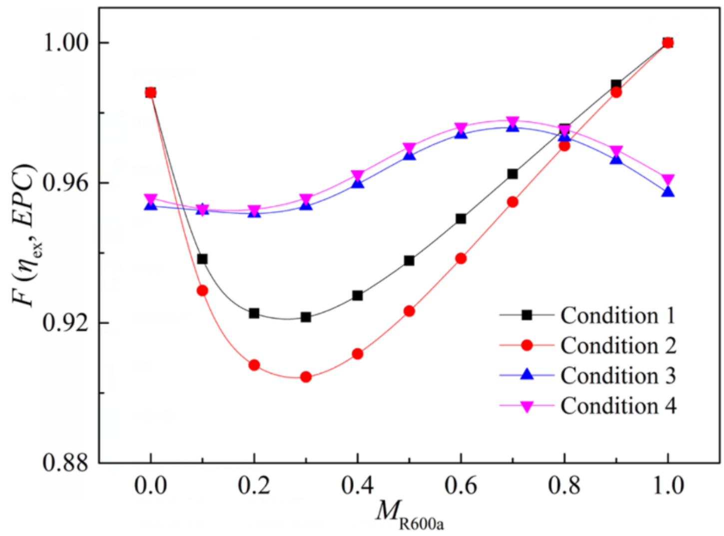

Figure 18. Change of $F(\eta_{ex}, EPC)$ with M_{R600a} under optimal crucial parameters.

Table 8. Performance comparison of four operational conditions under optimal crucial parameters.

Conditions	M_{R600a}	T_{11} (K)	W_{net} (kW)	η_{ex} (%)	*EPC* ($/kWh)
1 2	1	366.9	1651.2	51.85	0.1027
3	0.7	369.2	1670.6	53.91	0.1076
4		364.3	1759.7	53.67	0.1088

As demonstrated in Table 8, condition 4 has the lowest T_{11} and the largest W_{net} in four operational conditions, which denotes that the WHR rate of condition 4 is the maximum at a respectable 49.14%, showing the better energy-saving effect. Compared with condition 3 and condition 4, condition 1 and condition 2 using the pure OWM of R600a have the smallest *EPC*, showing the better economic performance. Furthermore, the condition 3 has the largest η_{ex}, but the T_{11} of condition 3 is the highest in four operational conditions, which leads to the conclusion that the WHR rate of condition 3 is 3.5% lower than that of condition 4. In addition, the W_{net}, η_{ex}, and *EPC* of conditions 3 and 4 are significantly greater than those of conditions 1 and 2, which denotes that the ORC system using the mixed OWM can achieve better energy and exergy performances by setting the saturated vapor temperature during the condensation process as the CT of OWM, while the ORC system using the pure OWM can achieve better economic performance.

4. Conclusions

Based on the goal of recycling low-grade waste heat efficiently, the LFG emitted from the sinter waste heat boiler is taken as the ORC heat source in the current study, and the energy, exergy, and economic models of the ORC system under four operational conditions are established. Then, the effects of M_{R600a} and ORC crucial parameters on the energy, exergy, and economic performances under four operational conditions are investigated, and the optimal variable parameters under four operational conditions are determined. The major findings are given below.

(1) The slip temperature of mixed OWM first rises and then reduces in both the evaporating and condensing processes as the M_{R600a} rises and steadily reduces as the ET and CT of OWM rise, while the SD of OWM has no effect on the slip temperature of mixed OWM. For a fixed M_{R600a}, the slip temperature of mixed OWM during the condensation process is greater than that during the evaporation process, and the slip temperature at the saturated liquid temperature is less than that at the saturated vapor temperature.

(2) As the M_{R600a} rises, the W_{net} and η_{ex} first rise and then reduce for the CT of the OWM set as the saturated vapor temperature during the condensation process, and first

reduce and then rise for the CT of the OWM set as the saturated liquid temperature during the condensation process. When the M_{R600a} is constant, the W_{net} first rises and then reduces with raising the ET of OWM for a certain condition, while the η_{ex} steadily rises. As the CT and SD of OWM rise, both the W_{net} and η_{ex} steadily reduce. Compared with the pure OWM, the ORC system using the mixed OWM can achieve the larger W_{net} and η_{ex} for the CT of the OWM set as the saturated vapor temperature during the condensation process. The W_{net} of condition 4 and the η_{ex} of condition 3 are the maximum in four operational conditions, showing better energy and exergy performances.

(3) The *EPC* first rises and then reduces as the M_{R600a} rises for a certain condition and steadily reduces with rising the ET of OWM. The *EPC*s of condition 1 and condition 2 rises with raising the CT of OWM, while the *EPC*s of condition 3 and condition 4 first rises and then reduces. As the SD of OWM rises, the *EPC* of condition 1 steadily rises, while the *EPC*s of the other three operational conditions first reduce and then rise. Compared with the other three conditions, the *EPC* of condition 3 is the minimum in four operational conditions when the CT of OWM is greater than 309.15 K, and the ORC system using the pure OWM of R601a can achieve the smallest *EPC* in four operational conditions, showing better economic performance.

(4) By taking the LFG of 453.15 K as the heat source of the ORC system, the optimal M_{R600a} in mixed OWM for both condition 3 and condition 4 is 0.7, and condition 1 and condition 2 using the pure OWM of R600a can achieve better overall performance. When the ET and CT of OWM are 393.15 K and 308.15 K, respectively, and the state of OWM at the evaporator outlet is the saturated vapor, the ORC systems of four operational conditions can achieve better overall performance. In four operational conditions, condition 4 has the largest W_{net}, and the WHR rate is 49.14%, which is also the maximum, showing the better energy-saving effect, while condition 3 has the largest η_{ex}, showing the better energy and exergy performances. Furthermore, condition 1 and condition 2 have the smallest *EPC*, showing the better economic performance.

Author Contributions: All authors contributed to this research in collaboration. J.F. and Y.Y. established the calculation model and finished the writing of the original draft; L.Z. conducted the data management and analysis; and H.D. provided substantial help with the paper schedule. All authors have read and agreed to the published version of the manuscript.

Funding: The authors gratefully acknowledge the financial support for this work provided by the National Natural Science Foundation of China (51974087), Anhui Provincial Natural Science Foundation (1908085QE203), and University Natural Science Research Foundation of Anhui Province (2022AH050262).

Institutional Review Board Statement: Not applicable.

Informed Consent Statement: Not applicable.

Data Availability Statement: The data presented in this study are available on request from the corresponding author.

Conflicts of Interest: The authors declare no conflicts of interest.

Nomenclature

A	Heat exchanging area (m^2)
c	specific heat (J/(kg·K))
h	specific enthalpy (kJ/kg)
m	mass flow rate (kg/s)
M	mass fraction
Q	Heat exchanging quantity (kW)
U	overall heat transfer coefficient (W/(m^2·K))
W_e	power output in expander (kW)
W_{net}	system net power output (kW)

W_p	power consumption in pump (kW)
T	temperature (K)
T_0	ambient temperature (K)
Greek symbols	
α, β	weighted coefficient
η_p	isentropic pump efficiency
η_e	isentropic expander efficiency
η_{ex}	exergy efficiency
ΔT_m	logarithmic mean temperature difference (K)
ΔT_{sup}	superheat degree (K)
Abbreviations	
CT	condensing temperature
EPC	electricity production cost
ET	evaporating temperature
LMTD	logarithmic mean temperature difference
LFG	low-grade flue gas
ORC	organic Rankine cycle
OWM	organic working medium
SD	superheat degree
THA	total heat exchanging area
WIC	whole investment cost
WHR	waste heat recovery
Subscripts	
1, 2, 3, ..., 14	state points shown in Figures 1 and 2
con	condenser
cond	condensing process
eva	evaporator
evap	evaporating process
f	working fluid
g	flue gas
prec	precooling process
preh	preheating process
suph	superheating process
tot	total
w	cooling water

References

1. Chen, W.D.; Huang, Z.F.; Chua, K.J. Sustainable energy recovery from thermal processes: A review. *Energy Sustain. Soc.* **2022**, *12*, 46. [CrossRef]
2. Ren, M.; Lu, P.T.; Liu, X.R.; Hossain, M.S.; Fang, Y.R.; Hanaoka, T.; O'Gallachoir, B.; Glynn, J.; Dai, H.C. Decarbonizing China's iron and steel industry from the supply and demand sides for carbon neutrality. *Appl. Energy* **2021**, *298*, 117209. [CrossRef]
3. Yin, R.Y.; Liu, Z.D.; Shangguan, F.Q. Thoughts on the implementation path to a carbon peak and carbon neutrality in China's steel industry. *Engineering* **2021**, *7*, 1680–1683. [CrossRef]
4. Ja'fari, M.; Khan, M.I.; Al-Ghamdi, S.G.; Jaworski, A.J.; Asfand, F. Waste heat recovery in iron and steel industry using organic Rankine cycles. *Chem. Eng. J.* **2023**, *477*, 146925. [CrossRef]
5. Köse, Ö.; Koç, Y.; Yağlı, H. Is Kalina cycle or organic Rankine cycle for industrial waste heat recovery applications? A detailed performance, economic and environment based comprehensive analysis. *Process Saf. Environ.* **2022**, *163*, 421–437. [CrossRef]
6. Daniarta, S.; Kolasiński, P.; Imre, A.R. Thermodynamic efficiency of trilateral flash cycle, organic Rankine cycle and partially evaporated organic Rankine cycle. *Energy Convers. Manag.* **2021**, *249*, 114731. [CrossRef]
7. Akimoto, R.; Yamaki, T.; Nakaiwa, M.; Matsuda, K. Evaluation of a power generation system that integrates multiple Kalina cycles and absorption heat pumps. *Case Stud. Therm. Eng.* **2021**, *28*, 101363. [CrossRef]
8. Garcia, S.I.; Garcia, R.F.; Carril, J.C.; Garciac, D.I. A review of thermodynamic cycles used in low temperature recovery systems over the last two years. *Renew. Sustain. Energy Rev.* **2018**, *81*, 760–767. [CrossRef]
9. Moreira, L.F.; Arrieta, F.R.P. Thermal and economic assessment of organic Rankine cycles for waste heat recovery in cement plants. *Renew. Sustain. Energy Rev.* **2019**, *114*, 109315. [CrossRef]
10. Pilia, R.; García Martíneza, L.; Wielandab, C.; Spliethoff, H. Techno-economic potential of waste heat recovery from German energy intensive industry with organic Rankine cycle technology. *Renew. Sustain. Energy Rev.* **2020**, *134*, 110324. [CrossRef]

11. Loni, R.; Najafi, G.; Bellos, E.; Rajaee, F.; Said, Z.; Mazlan, M. A review of industrial waste heat recovery system for power generation with Organic Rankine Cycle: Recent challenges and future outlook. *J. Clean. Prod.* **2021**, *287*, 125070. [CrossRef]
12. Li, P.C.; Cao, Q.; Li, J.; Lin, H.W.; Wang, Y.D.; Gao, G.T.; Pei, G.; Jie, D.S.; Liu, X.F. An innovative approach to recovery of fluctuating industrial exhaust heat sources using cascade Rankine cycle and two-stage accumulators. *Energy* **2021**, *228*, 120587. [CrossRef]
13. Wang, D.X.; Ling, X.; Peng, H.; Liu, L.; Tao, L.L. Efficiency and optimal performance evaluation of organic Rankine cycle for low grade waste heat power generation. *Energy* **2013**, *50*, 343–352. [CrossRef]
14. Cataldo, F.; Mastrullo, R.; Mauro, A.W.; Vanoli, G.P. Fluid selection of Organic Rankine Cycle for low-temperature waste heat recovery based on thermal optimization. *Energy* **2014**, *72*, 159–167. [CrossRef]
15. Xu, H.; Gao, N.P.; Zhu, T. Investigation on the fluid selection and evaporation parametric optimization for sub- and supercritical organic Rankine cycle. *Energy* **2016**, *96*, 59–68. [CrossRef]
16. Fergani, Z.; Touil, D.; Morosuk, T. Multi-criteria exergy based optimization of an Organic Rankine Cycle for waste heat recovery in the cement industry. *Energy Convers. Manag.* **2016**, *112*, 81–90. [CrossRef]
17. Li, J.; Liu, Q.; Ge, Z.; Duan, Y.Y.; Yang, Z. Thermodynamic performance analyses and optimization of subcritical and transcritical organic Rankine cycles using R1234ze(E) for 100–200 °C heat sources. *Energy Convers. Manag.* **2017**, *14*, 140–154. [CrossRef]
18. Mohammadkhani, F.; Yari, M. A 0D model for diesel engine simulation and employing a transcritical dual loop Organic Rankine Cycle (ORC) for waste heat recovery from its exhaust and coolant: Thermodynamic and economic analysis. *Appl. Therm. Eng.* **2019**, *150*, 329–347. [CrossRef]
19. Ping, X.; Yao, B.F.; Zhang, H.G.; Yang, F.B. Thermodynamic, economic, and environmental analysis and multi-objective optimization of a dual loop organic Rankine cycle for CNG engine waste heat recovery. *Appl. Therm. Eng.* **2021**, *193*, 116980. [CrossRef]
20. Liang, Y.C.; Bian, X.Y.; Qian, W.W.; Pan, M.Z.; Ban, Z.B.; Yu, Z.B. Theoretical analysis of a regenerative supercritical carbon dioxide Brayton cycle/organic Rankine cycle dual loop for waste heat recovery of a diesel/natural gas dual-fuel engine. *Energy Convers. Manag.* **2019**, *197*, 111845. [CrossRef]
21. Yang, A.; Su, Y.; Shen, W.F.; Chien, I.L.; Ren, J.Z. Multi-objective optimization of organic Rankine cycle system for the waste heat recovery in the heat pump assisted reactive dividing wall column. *Energy Convers. Manag.* **2019**, *199*, 112041. [CrossRef]
22. Wang, Y.L.; Yang, H.D.; Xu, K.K. Comparative environmental impacts and emission reductions of introducing the novel organic Rankine & Kalina cycles to recover waste heat for a roller kiln. *Appl. Therm. Eng.* **2021**, *190*, 116821.
23. Feng, Y.Q.; Hung, T.C.; Zhang, Y.N.; Li, B.X.; Yang, J.F.; Shi, Y. Performance comparison of low-grade ORCs (organic Rankine cycles) using R245fa, pentane and their mixtures based on the thermo-economic multi-objective optimization and decision makings. *Energy* **2015**, *93*, 2018–2029. [CrossRef]
24. Liu, Q.; Shen, A.J.; Duan, Y.Y. Parametric optimization and performance analyses of geothermal organic Rankine cycles using R600a/R601a mixtures as working fluids. *Appl. Energy* **2015**, *148*, 410–420. [CrossRef]
25. Li, Z.S.; Li, W.Y.; Xu, B.R.; Jia, X.D.; Jiang, J. Performance research of combined cooling heat and power-organic Rankine cycle system installed with heat pump using mixtures. *Proc. CSEE* **2015**, *35*, 4972–4980.
26. Pang, K.C.; Chen, S.C.; Hung, T.C.; Feng, Y.Q.; Yang, S.C.; Wong, K.W.; Lin, J.R. Experimental study on organic Rankine cycle utilizing R245fa, R123 and their mixtures to investigate the maximum power generation from low-grade heat. *Energy* **2017**, *133*, 636–651. [CrossRef]
27. Feng, Y.Q.; Hung, T.C.; He, Y.L.; Wang, Q.; Wang, S.; Li, B.X.; Lin, J.R.; Zhang, W.P. Operation characteristic and performance comparison of organic Rankine cycle (ORC) for low-grade waste heat using R245fa, R123 and their mixtures. *Energy Convers. Manag.* **2017**, *144*, 153–163. [CrossRef]
28. Su, W.; Hwang, Y.H.; Deng, S.; Zhao, L.; Zhao, D.P. Thermodynamic performance comparison of organic Rankine cycle between zeotropic mixtures and pure fluids under open heat source. *Energy Convers. Manag.* **2018**, *165*, 720–737. [CrossRef]
29. Dong, B.S.; Xu, G.Q.; Li, T.T.; Quan, Y.K.; Wen, J. Thermodynamic and economic analysis of zeotropic mixtures as working fluids in low temperature organic Rankine cycles. *Appl. Therm. Eng.* **2018**, *132*, 545–553. [CrossRef]
30. Fang, Y.W.; Yang, F.B.; Zhang, H.G. Comparative analysis and multi-objective optimization of organic Rankine cycle (ORC) using pure working fluids and their zeotropic mixtures for diesel engine waste heat recovery. *Appl. Therm. Eng.* **2019**, *157*, 113704. [CrossRef]
31. Miao, Z.; Li, Z.H.; Zhang, K.; Xu, J.L.; Cheng, Y.P. Selection criteria of zeotropic mixtures for subcritical organic Rankine cycle based on thermodynamic and economic analysis. *Appl. Therm. Eng.* **2020**, *180*, 115837. [CrossRef]
32. Xi, H.; Li, M.J.; He, Y.L.; Zhang, Y.W. Economical evaluation and optimization of organic Rankine cycle with mixture working fluids using R245fa as flame retardant. *Appl. Therm. Eng.* **2017**, *113*, 1056–1070. [CrossRef]
33. Zhi, L.H.; Hu, P.; Chen, L.X.; Zhao, G. Performance analysis and optimization of engine waste heat recovery with an improved transcritical-subcritical parallel organic Rankine cycle based on zeotropic mixtures. *Appl. Therm. Eng.* **2020**, *181*, 115991. [CrossRef]
34. Li, J.; Yang, Z.; Hu, S.Z.; Yang, F.B.; Duan, Y.Y. Economic performance improvement of butane/isopentane mixtures in organic Rankine cycles by liquid-separated condensation method. *Appl. Therm. Eng.* **2020**, *181*, 115941. [CrossRef]
35. Tian, Z.; Zeng, W.J.; Gu, B.; Zhang, Y.; Yuan, X. Energy, exergy, and economic (3E) analysis of an organic Rankine cycle using zeotropic mixtures based on marine engine waste heat and LNG cold energy. *Energy Convers. Manag.* **2021**, *228*, 113657. [CrossRef]

36. Andreasen, J.G.; Baldasso, E.; Kærn, M.R.; Weith, T.; Heberle, F.; Brüggemann, D.; Haglind, F. Techno-economic feasibility analysis of zeotropic mixtures and pure fluids for organic Rankine cycle systems. *Appl. Therm. Eng.* **2021**, *192*, 116791. [CrossRef]
37. Wang, E.H.; Zhang, M.R.; Meng, F.X.; Zhang, H.G. Zeotropic working fluid selection for an organic Rankine cycle bottoming with a marine engine. *Energy* **2022**, *243*, 123097. [CrossRef]
38. Ma, W.W.; Liu, T.; Min, R.; Li, M. Effects of physical and chemical properties of working fluids on thermodynamic performances of medium-low temperature organic Rankine cycles (ORCs). *Energy Convers. Manag.* **2018**, *171*, 742–749. [CrossRef]
39. Feng, J.S.; Pei, G.; Dong, H.; Zhang, S. Performance analysis of organic Rankine cycle power generation system with sinter cooling gas waste heat. *J. Cent. South Univ. (Sci. Technol.)* **2019**, *50*, 466–473.
40. Feng, J.S.; Gao, G.T.; Dabwan, Y.N.; Pei, G.; Dong, H. Thermal performance evaluation of subcritical organic Rankine cycle for waste heat recovery from sinter annular cooler. *J. Iron Steel Res. Int.* **2020**, *27*, 248–258. [CrossRef]
41. Feng, J.S.; Cheng, X.N.; Wang, H.H.; Zhao, L.; Dong, H. Effect of flue gas outlet temperature in evaporator on thermal economic performance of organic Rankine cycle system for sinter waste heat recovery. *J. Iron Steel Res. Int.* **2023**, *30*, 2378–2390. [CrossRef]
42. Chen, W.J.; Feng, H.J.; Chen, L.G.; Xia, S.J. Optimal performance characteristics of subcritical simple irreversible organic Rankine cycle. *J. Therm. Sci.* **2018**, *27*, 555–562. [CrossRef]
43. Liu, Y.L.; Zhang, C.; Zou, Y.P.; Chen, J.; Liu, C. Thermal-economic evaluation of using organic Rankine cycle system to recover flue gas waste heat of a 30t/h industrial boiler. *J. Chongqing Univ.* **2018**, *41*, 91–99.
44. Li, T.L.; Gao, R.Z.; Gao, X. Energy, exergy, economic, and environment (4E) assessment of trans-critical organic Rankine cycle for combined heating and power in wastewater treatment plant. *Energy Convers. Manag.* **2022**, *267*, 115932. [CrossRef]
45. Wang, Q.L.; Wang, J.Q.; Li, T.L.; Meng, N. Techno-economic performance of two-stage series evaporation organic Rankine cycle with dual-level heat sources. *Appl. Therm. Eng.* **2020**, *171*, 115078. [CrossRef]
46. Mignard, D. Correlating the chemical engineering plant cost index with macro-economic indicators. *Chem. Eng. Res. Des.* **2014**, *92*, 285–294. [CrossRef]
47. Wang, J.Y.; Wang, W.B. Comprehensive analysis and multi-objective optimization of organic rankine cycle power generation system based on waste heat utilization between compressor stages. *J. Shanxi Univ. Sci. Technol.* **2023**, *41*, 165–171.
48. Nafey, A.S.; Sharaf, M.A. Combined solar organic Rankine cycle with reverse osmosis desalination process: Energy, exergy, and cost evaluations. *Renew. Energy* **2010**, *35*, 2571–2580. [CrossRef]
49. Samadi, F.; Kazemi, N. Exergoeconomic analysis of zeotropic mixture on the new proposed organic Rankine cycle for energy production from geothermal resources. *Renew. Energy* **2020**, *152*, 1250–1265. [CrossRef]
50. Liao, G.L.; E, J.Q.; Zhang, F.; Chen, J.W.; Leng, E.W. Advanced exergy analysis for Organic Rankine Cycle-based layout to recover waste heat of flue gas. *Appl. Energy* **2020**, *266*, 114891. [CrossRef]
51. Lu, J.L.; Zhang, J.; Chen, S.L.; Pu, Y.M. Analysis of organic Rankine cycles using zeotropic mixtures as working fluids under different restrictive conditions. *Energy Convers. Manag.* **2016**, *126*, 704–716. [CrossRef]